Continuum approach for modelling transversely isotropic high-cycle fatigue ☆

Sami Holopainen*, Reijo Kouhia, Timo Saksala

Tampere University of Technology
Department of Mechanical Engineering and Industrial Systems
P.O. Box 589, FI-33101 Tampere, Finland

Abstract

A continuum approach is proposed for modelling multiaxial high-cycle fatigue of solids which exhibit transversely isotropic fatigue properties. The approach is an extension of the original isotropic model proposed by Ottosen, Stenström and Ristinmaa in 2008, which model is based on the concept of a moving endurance surface in the stress space and on an evolving damage variable. The theory is formulated in a rate form within continuum mechanics framework without the need to measure damage changes per loading cycles. Capability of the approach is illustrated by several examples with different uni- and multiaxial loading histories.

Keywords: high-cycle fatigue, transversely isotropic fatigue, out-of-phase loading

1. Introduction

Design against fatigue constitutes an integral part of mechanical engineering analysis. Examples of mechanical components that experience fatigue during their service life are axels in motors, railroad wheels, aircraft components, crankshafts, propellor shafts, and turbine blends to mention a few. As expressed by Bolotin (1999), in the narrow sense the term fatigue of materials and structural components means damage and fracture due to cyclic, repeatedly applied stress. It has been recognized in practise that the fatigue stress conditions are often multiaxial consisting of combined bending and twisting, and the conditions can additionally be of out-of-phase and subjected to different frequencies. Under those alternating complex loadings, material fails at stress levels substantially lower than observed under monotonic loadings. To understand and model

☆Accepted, June 2016
*Corresponding author
Email addresses: sami.holopainen@tut.fi (Sami Holopainen), reijo.kouhia@tut.fi (Reijo Kouhia), timo.saksala@tut.fi (Timo Saksala)

fatigue phenomena under different loading situations, knowledge from materials science and mechanics of solids is mandatory, cf, e.g. Suresh (1998), Murakami (2002).

High-cycle fatigue, which typically occurs when the loading consists more than of 10^4 cycles and the macroscopic behaviour of the material is primarily elastic, is influenced by several factors such as surface roughness, grain size and distribution as well as cleanliness of material, cf. Morel (2001), Morel et al. (2001), and Makkonen et al. (2014). Subjected to those metallurgical variables, material undergoes fatigue damage which is associated to degradation of material properties due to initiation, growth, and coalescence of microdefects. If the defects in the material are assumed to be distributed in a statistically homogeneous manner then it is advantageous to model the fatigue mechanisms within continuum mechanics framework. The specific features with regard to continuum damage mechanics and fatigue are discussed e.g. in Paas et al. (1993) and Wang and Yao (2004). Moreover, the fundamental ingredients of dynamic failures, high-cycle fatigue, ductile failure, and failure of brittle and quasi-brittle materials are found e.g. from McDowell (1996), Lemaitre and Desmorat (2005), Desmorat et al. (2007), and Murakami (2012).

Basically three stages can be identified in the process of fatigue failure, cf. Lemaitre (1984), Suresh (1998), Morel et al. (2001): (i) nucleation and growth of micro-cracks and voids due to local inhomogeneities and local micro-plastic effects terminating in the creation of macro-cracks; (ii) stable crack propagation phase; (iii) unstable crack propagation phase leading to failure. In uniaxial fatigue tests, the phase (ii) can further be divided into two stages: (a) crack growth on a plane of maximum shear and (b) crack propagation normal to the tensile stress. However, most of the fatigue life is spent in the stage (i). The goal of the present work is to find a representative continuum-based model capable to predict macroscopic mechanical behaviour which mainly results from micro-cracking during the first stage (i). In contrast to the last two stages which are dominated by macro-cracks, the first stage is governed by statistically distributed micro-mechanisms. Due to this characteristic, linear fracture mechanics cannot be applied in the first stage.

Different approaches for fatigue analysis exist, cf. Sines (1955), Findley (1959), Dang Van et al. (1989), Dang Van (1993), Palin-Luc and Lasserre (1998), Papadopoulos (2001), Socie and Marquis (2000), Zouain and Cruz (2002), Liu and Zenner (2003), and Zhang et al. (2012). Since entire high-cycle fatigue process relies on brittle damage mechanisms, strain controlled approaches suitable for ductile damage behaviour cannot be directly applied, and stress-based approaches are preferred, cf. Ottosen et al. (2008). Majority of those approaches represents fatigue-limit criteria, cumulative damage theories, and cycle-counting methods. Among fatigue-limit criteria, critical plane approaches have gained a large popularity meanwhile equivalent, invariant, and average stress approaches represent other prominent examples in more early stage on the research.

According to critical plane approaches, fatigue life is controlled by combined action of alternating shear stresses and the normal stress acting on a plane. This plane, which is termed the critical plane, varies between models. Perhaps the

pioneering model by Findley (1959) is one of the most used high-cycle fatigue criterion. One more recent state-of-the-art example of critical plane approaches is the multiaxial fatigue criteria model for metals given by Liu and Mahadevan (2007). Other representative approaches are found e.g in Matake (1977), Dang Van (1993), Carpinteri and Spagnoli (2001), and Papadopoulos (2001).

Two shortcomings of the critical plane approaches are the inability of the defined critical plane to follow crack initiation realistically and the restriction only to a certain set of material parameters. The latter feature is due to a critical plane which only accounts for the stress state, but not material properties.

All the previously mentioned invariant based and critical plane fatigue-limit criteria describe the fatigue limits under infinite number of identical cycles. However, for finite life predictions those models are equipped with cumulative damage theories, which describe the damage increase per cycle. Due to this characteristic, the loading is required to consist of well-defined cycles. Probably the best known model among the cumulative damage theories is the Palmgren-Miner model.

To model fatigue under complex load histories, cycle-counting methods need to be applied so as to define equivalent, representative cycles. However, definition of equivalent cycles from a complex load spectrum is a challenging task which feature makes the cycle-counting approaches difficult to apply in practice.

A notable contribution for general computational high-cycle fatigue analysis is given by Peerlings et al. (2000), who proposed a continuum damage model for the prediction of crack initiation and propagation. They also showed that the damage growth localizes in a vanishing volume which is due to the singularity of the damage rate at the crack tip. To remove the damage rate singularity, Peerlings et al. (2000) proposed a gradient-enhancement to their constitutive model. More recent investigations of gradient effects on fatigue are found e.g. in studies by Askes et al. (2012) and Luu et al. (2014).

Although a multitude of models for multiaxial fatigue damage have already been proposed, many of them are not able to predict fatigue under complex and out-of-phase loadings well. Many models in the early stage in the research cannot satisfactorily represent the fatigue life for more than 10^6 either, or they initially are conceived only for in-phase cyclic stresses, i.e. proportional cyclic loadings are required. Reviews and comparisons of different high-cycle fatigue models can be found in studies by Papadopoulos et al. (1997), Ding et al. (2007), Kenmeugne et al. (2012), and Lorand (2012). Furthermore, research related to anisotropic fatigue models has mainly been focused on uniaxially reinforced, transversely isotropic composites for which the elasticity properties also are transversely isotropic, cf. Robinson and Duffy (1990); Robinson et al. (1990); Arnold and Kruch (1991); Kruch and Arnold (1997). Although mechanical behaviour of many materials can be considered elastically isotropic, their fatigue properties may differ in different directions. An example of such material is forged steel whose fatigue properties are transversally isotropic. Majority of the models discussed above cannot be applied to the modelling of anisotropic fatigue behaviour or they are formulated using cycle-counting methodologies generally unsuitable in demanding practical applications.

An appealing model for high-cycle fatigue suitable for arbitrary multiaxial loadings was proposed by Ottosen et al. (2008). In their approach, the concept of a moving endurance surface in the stress space is postulated together with a damage evolution equation. Movement of the endurance surface is modeled with a reduced deviatoric stress measure which defines the center of the endurance surface in a similar way than the back-stress tensor in plasticity, thus memorizing the load history. Damage evolution is activated whenever the stress state is outside the endurance surface, and the time rate of the endurance surface is positive. In this model, uniaxial and multiaxial stress states are treated in a unified manner for arbitrary loading histories, thus avoiding cycle-counting techniques. Therefore, the approach by Ottosen et al. (2008) could be described as an evolution equation based fatigue model. It has been also used in a recent study by Brighenti et al. (2013). Similar features can also be observed in the approaches proposed by Peerlings et al. (2000), Morel et al. (2001), and Zouain et al. (2006).

In this paper, a transversely isotropic high-cycle fatigue model is presented. Consistent with the Ottosen et al. (2008) approach, the proposed model is formulated using evolution equations which feature makes the definition of damage changes per cycle redundant, i.e. cycle-counting techniques do not need to be applied. Compared to preceding approaches of similar concept, the model uses only macroscopical quantities, which property makes the model simpler.

2. The model

2.1. Isotropic high-cycle fatigue (HCF) model

In this section, the model concept of the approach developed by Ottosen et al. (2008) for isotropic solids is briefly summarized. The model uses only macroscopical quantities, and the constitutive response is assumed to be purely elastic, which is a relevant feature in macroscopic HCF-modelling. It is well known that the endurance limits of a material change with load conditions and that loading within these limits do not necessarily result in damage development. Based on these features Ottosen et al. (2008) postulated an endurance surface β in the stress space as

$$\beta = \frac{1}{S_0}(\bar{\sigma} + AI_1 - S_0) = 0. \tag{1}$$

Denoting the stress tensor as $\boldsymbol{\sigma}$, the first stress invariant is given by $I_1 = \operatorname{tr}\boldsymbol{\sigma}$. The invariant I_1 reflects the effect of the mean stress, i.e. the hydrostatic tension enhances the fatigue development while fatigue is suppressed under hydrostatic compression. The parameter A is considered as positive and non-dimensional, and can be associated in uniaxial cyclic loading as the slope of the Haigh-diagram. The last parameter S_0 is the endurance limit for zero mean stress. The effective stress present in (1) is defined in terms of the second invariant of the reduced deviatoric stress $\boldsymbol{s} - \boldsymbol{\alpha}$ as

$$\bar{\sigma} = \sqrt{3J_2(\boldsymbol{s} - \boldsymbol{\alpha})} = \sqrt{\tfrac{3}{2}(\boldsymbol{s} - \boldsymbol{\alpha}) \mathbf{:} (\boldsymbol{s} - \boldsymbol{\alpha})} =: \sqrt{\frac{3}{2}}\|\boldsymbol{s} - \boldsymbol{\alpha}\|, \tag{2}$$

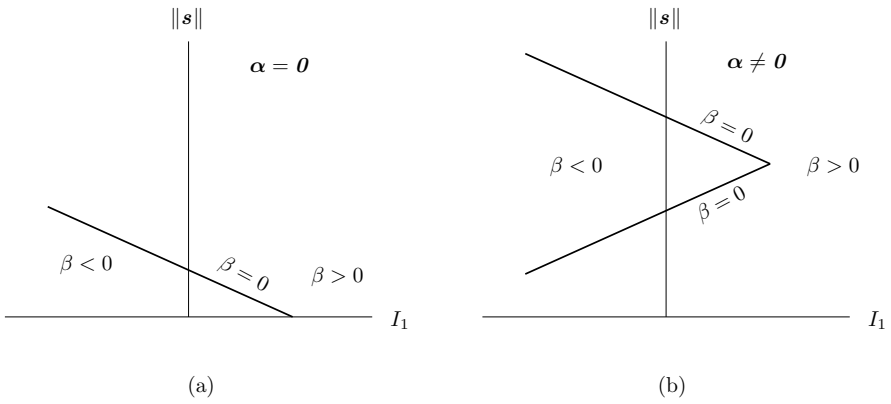

Figure 1: Endurance surface presented in a meridian plane as the backstress is (a) $\boldsymbol{\alpha} = \boldsymbol{0}$ and (b) $\boldsymbol{\alpha} \neq \boldsymbol{0}$.

where $\boldsymbol{s} = \boldsymbol{\sigma} - \frac{1}{3}\mathrm{tr}\,(\boldsymbol{\sigma})\boldsymbol{I}$ is the deviatoric stress tensor and $\boldsymbol{I}$ stands for the identity tensor. The operator **:** denotes the double dot product between two second order tensors, i.e. $\boldsymbol{A} : \boldsymbol{B} := \mathrm{tr}\,(\boldsymbol{A}\boldsymbol{B}^T)$.

Shape of the endurance surface in the deviatoric plane is circular and the meridian lines are straight as with the case of the Drucker-Prager model in plasticity, cf. Fig. 1. The center point in the deviatoric plane is defined by the $\boldsymbol{\alpha}$-tensor, which memorizes the load history and results in the movement of the endurance surface in the stress space.

For the evolution of the deviatoric back-stress tensor $\boldsymbol{\alpha}$, a hardening rule similar to Ziegler's kinematic hardening rule in plasticity theory is adopted, i.e.

$$\dot{\boldsymbol{\alpha}} = C(\boldsymbol{s} - \boldsymbol{\alpha})\dot{\beta}, \tag{3}$$

where C is a non-dimensional material parameter, and the dot denotes the time rate.

Despite damage resulting principally from the initiation, nucleation, and growth of voids and micro-cracks generate anisotropic behaviour, material damage is formulated from a macroscopic viewpoint by using an isotropic measure $D \in [0, 1]$, for which the evolution is governed by the equation of the form

$$\dot{D} = g(\beta, D)\dot{\beta}, \quad g(\beta \geq 0, D) \geq 0. \tag{4}$$

The specific form of the function g will be discussed subsequently. Since $g \geq 0$ and damage never decreases, it then follows that for damage evolution $\dot{\beta} \geq 0$. A glance at (3) also reveals that the evolution of the back-stress takes place only if the conditions

$$\beta \geq 0 \quad \text{and} \quad \dot{\beta} > 0 \tag{5}$$

are satisfied.

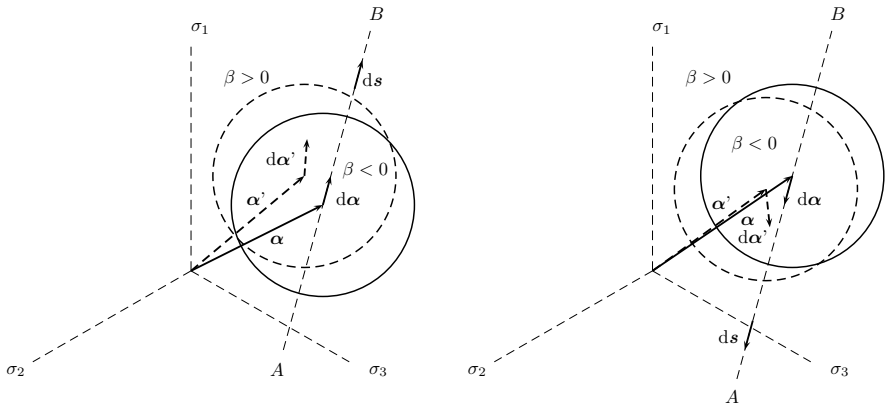

Figure 2: Alternating stress state. The endurance surface will track the current stress state and then it moves between the states A and B (generally not fixed). The initial and final state are highlighted by the dashed and solid line, respectively.

In contrast to plasticity, the stress state can lie outside the endurance surface. When the stress state is outside the endurance surface and moves away from this surface, $\dot{D} \geq 0$ and $\dot{\boldsymbol{\alpha}} \neq 0$ according to (3), (4) and (5). Otherwise the endurance surface does not move, i.e. $\dot{D} = 0$ and $\dot{\boldsymbol{\alpha}} = \boldsymbol{0}$. As an example, considering a specific, periodically alternating stress state. Initially, the endurance surface moves in a different manner over each cycle. During loading, however, the endurance surface rapidly tracks the stress state since the direction of the movement always is $\boldsymbol{s} - \boldsymbol{\alpha}$. Fig. 2 illustrates the situation when $\dot{\boldsymbol{\alpha}} \neq 0$ and an alternating stress state is applied.

2.2. Integrity basis for transverse isotropy

A transversely isotropic solid is characterized by a unit vector $\boldsymbol{b}$ in the privileged direction and an isotropic plane perpendicular to it. The most general form of an endurance surface can depend on the following five tensor invariants, cf. Boehler (1987),

$$I_1 = \operatorname{tr} \boldsymbol{\sigma}, \quad I_2 = \tfrac{1}{2} \operatorname{tr} \boldsymbol{\sigma}^2, \quad I_3 = \tfrac{1}{3} \operatorname{tr} \boldsymbol{\sigma}^3, \quad I_4 = \operatorname{tr} (\boldsymbol{\sigma} \boldsymbol{B}), \quad I_5 = \operatorname{tr} (\boldsymbol{\sigma}^2 \boldsymbol{B}), \tag{6}$$

where $\boldsymbol{B} = \boldsymbol{b} \otimes \boldsymbol{b}$ is the structural tensor for transverse isotropy. For further convenience, the invariants in terms of the stress deviator $\boldsymbol{s}$ are defined as

$$J_2 = \tfrac{1}{2} \operatorname{tr} (\boldsymbol{s}^2), \quad J_4 = \operatorname{tr} (\boldsymbol{s} \boldsymbol{B}), \quad J_5 = \operatorname{tr} (\boldsymbol{s}^2 \boldsymbol{B}). \tag{7}$$

In order to distinguish stresses from those that occur in the transverse isotropy plane, the stress tensor $\boldsymbol{\sigma}$ is additively decomposed as

$$\boldsymbol{\sigma} = \boldsymbol{\sigma}_{\mathrm{L}} + \boldsymbol{\sigma}_{\mathrm{T}}, \tag{8}$$

where $\boldsymbol{\sigma}_{\mathrm{T}}$ and $\boldsymbol{\sigma}_{\mathrm{L}}$ are termed the transverse and the longitudinal component, respectively. The transverse component $\boldsymbol{\sigma}_{\mathrm{T}}$ is obtained from the stress tensor $\boldsymbol{\sigma}$ by use of the projector tensor $\boldsymbol{P} = \boldsymbol{I} - \boldsymbol{B}$ as

$$\boldsymbol{\sigma}_{\mathrm{T}} = \boldsymbol{P}\boldsymbol{\sigma}\boldsymbol{P} = \boldsymbol{\sigma} - \boldsymbol{\sigma}\boldsymbol{B} - \boldsymbol{B}\boldsymbol{\sigma} + \boldsymbol{B}\boldsymbol{\sigma}\boldsymbol{B}. \tag{9}$$

The longitudinal component $\boldsymbol{\sigma}_{\mathrm{L}}$ simply follows from Eq. (8). It can be concluded that the stress component $\boldsymbol{\sigma}_{\mathrm{T}}$ is in the state of plane stress.

It is known that fatigue failure is also dependent on the maximum shear stresses occurring in the longitudinal planes and in the transverse isotropy plane. These quantities can be expressed in terms of the deviatoric invariants J_2, J_4, and J_5 as

$$\tau_{\mathrm{L}}^2 = J_5 - J_4^2, \tag{10}$$

$$\tau_{\mathrm{T}}^2 = J_2 + \tfrac{1}{4}J_4^2 - J_5. \tag{11}$$

Models presented in Refs. Robinson and Duffy (1990), Robinson et al. (1990), Arnold and Kruch (1991), and Kruch and Arnold (1997) exploit these invariants. Ramifications in model results due to those invariants are evidently of interest to study. To keep the model simple, however, the maximum shear stresses τ_{L} and τ_{T} have not been used in the proposed approach.

2.3. Transversely isotropic high-cycle fatigue model

Due to specific directional microstructural characteristics, many materials exhibit fatigue properties which are transversely isotropic. However, the approach chosen is purely phenomenological and is not aimed at a particular material with a specific microstructure. Thus, for such materials, an extension of the endurance surface (1) can be defined as

$$\beta = \frac{1}{S_{\mathrm{T}}}\left\{\bar{\sigma} + A_{\mathrm{L}} I_{\mathrm{L1}} + A_{\mathrm{T}} I_{\mathrm{T1}} - [(1-\zeta)S_{\mathrm{T}} + \zeta S_{\mathrm{L}}]\right\} = 0, \tag{12}$$

where the linear invariants of the longitudinal and transverse stress tensors are

$$I_{\mathrm{L1}} = \operatorname{tr}\boldsymbol{\sigma}_{\mathrm{L}} = I_4, \tag{13}$$

$$I_{\mathrm{T1}} = \operatorname{tr}\boldsymbol{\sigma}_{\mathrm{T}} = I_1 - I_4. \tag{14}$$

The effective stress $\bar{\sigma}$ is defined as in the isotropic case, see Eq. (2). In addition to the invariants, the parameter ζ is used to reflect the average loading direction defined in terms of the stress ratio

$$\zeta = \left(\frac{\boldsymbol{\sigma}_{\mathrm{L}} : \boldsymbol{\sigma}_{\mathrm{L}}}{\boldsymbol{\sigma} : \boldsymbol{\sigma}}\right)^n = \left(\frac{2I_5 - I_4^2}{2I_2}\right)^n \tag{15}$$

where n is a material parameter.

In the endurance surface there are four additional material parameters A_{L}, S_{L}, A_{T}, and S_{T} which have similar meaning as parameters A and S_0 in (1), i.e.

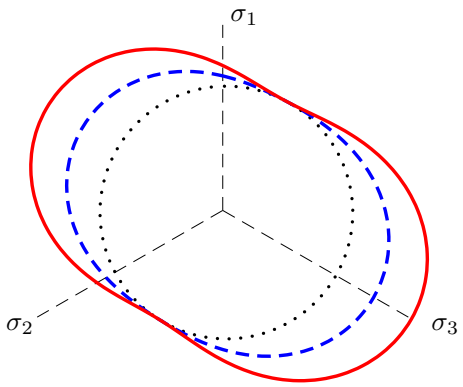

Figure 3: Endurance surface in the π-plane as the fatigue strength ratio is $S_{\text{L}}/S_{\text{T}} = 1$ (dotted black line), $S_{\text{L}}/S_{\text{T}} = 1.5$ (dashed blue line), and $S_{\text{L}}/S_{\text{T}} = 2$ (red solid line). The parameters employed are $A_{\text{L}} = 0.225$ and $A_{\text{T}} = 0.275$, and the unit vector is $\boldsymbol{b} = (0, 0, 1)^T$.

A_{L}, S_{L} and A_{T}, S_{T} correspond to the parameters A and S_0 if the cyclic stress is applied in longitudinal and transverse directions, respectively. Shape of the endurance surface in the π-plane is shown in Fig. 3. In contrast to isotropic failure when the locus of the endurance surface is circle on the deviatoric plane, the surface (12) will depart from convexity depending on the ratio $S_{\text{L}}/S_{\text{T}}$. However, it should be mentioned that the non-convexity is most pronounced on the π-plane.

When uniaxial loading in a direction $\boldsymbol{n}$ is applied, the ζ-parameter takes the following form

$$\zeta = (2\cos^2\psi - \cos^4\psi)^n, \tag{16}$$

where ψ is the angle between the loading and longitudinal directions $\boldsymbol{n}$ and $\boldsymbol{b}$, respectively ($\cos\psi = \boldsymbol{n} \cdot \boldsymbol{b}$). The dependence of the parameter ζ on n is shown in Fig. 4. Due to the lack of data in the intermediate directions, the value $n = 1$ has been used in this study since it fits rather well with the only available data in the direction $\psi = 45°$, see Fig. 4.

2.4. Damage evolution

What remains to be defined is an expression for the function g present in the damage evolution law (4). Despite the directionality of damage phenomena, the model is kept simple by describing damage by a scalar quantity D ranging between the values $0 \leq D \leq 1$, where 0 corresponds to undamaged state and 1 to fully damaged material state. It is well known for metallic materials that the rate of damage increases with growing damage, and therefore the following form

$$\dot{D} = g(\beta, D)\dot{\beta} := \frac{K}{(1-D)^k}\exp(L\beta)\dot{\beta} \tag{17}$$

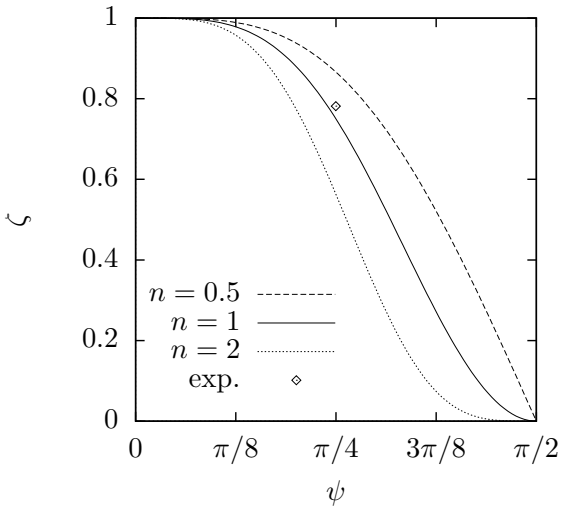

Figure 4: Dependence of the parameter ζ on the exponent n and the angle ψ between the loading and preferred longitudinal directions $\boldsymbol{n}$ and $\boldsymbol{b}$, respectively. The experimental result for the forged 34CrMo6 steel in the direction of 45° is also shown.

is chosen for the damage evolution law. In (17), k, K, and L are material parameters. Based on the damage models in Lemaitre and Chaboche (1990) and Lemaitre and Desmorat (2005) the value $k = 1$ has been used in the present study.

3. Calibration of the model

In what follows, a procedure to obtain the material parameters S_{L}, S_{T}, A_{L}, A_{T}, C, K, and L from a uniaxial test data is described. Under uniaxial stress states, the only nonzero stress component is $\sigma := \sigma_{11}$, while the relation between the backstress components is $\alpha := \alpha_{11} = -2\alpha_{22} = -2\alpha_{33}$. Hence, the effective stress (2) takes a simple form as

$$\bar{\sigma} = \kappa(\sigma - \frac{3}{2}\alpha) \tag{18}$$

where the parameter κ controls the sign, i.e. $\kappa = 1$ as $(\sigma - \frac{3}{2}\alpha) > 0$ and $\kappa = -1$ as $(\sigma - \frac{3}{2}\alpha) < 0$. Moreover, the endurance surface (12) in a meridian plane reduces to a single line given as

$$\beta = \frac{1}{S_{\text{T}}}\left\{\kappa(\sigma - \frac{3}{2}\alpha) + \tilde{A}\sigma - \tilde{S}_0\right\} = 0 \tag{19}$$

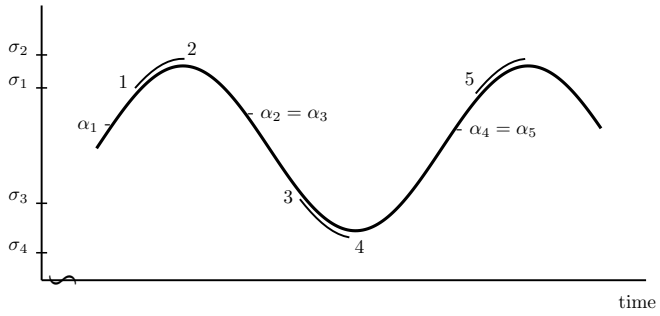

Figure 5: Periodically alternating uniaxial stress state. The damage development and movement of the endurance surface during cycling is indicated by a double curve.

where $\tilde{A}$ and $\tilde{S}_0$ have the following values in the loading direction ψ

$$\tilde{A} = A_{\mathrm{T}} + (A_{\mathrm{L}} - A_{\mathrm{T}}) \cos^2 \psi, \tag{20}$$

$$\tilde{S}_0 = (1 - \zeta) S_{\mathrm{T}} + \zeta S_{\mathrm{L}}, \tag{21}$$

and ζ is defined in (16).

Assuming a proportional loading where the stress varies linearly between arbitrary stress states $\boldsymbol{\sigma}(A)$ and $\boldsymbol{\sigma}(B)$ located on the opposite sides of the endurance surface, i.e. the stress path goes through the center of the endurance surface, see Fig. 2. Under this particular condition, it can be shown that the endurance surface (1) for isotropic fatigue will reduce to the fatigue criterion of Sines, cf. Sines (1955, 1959), and see Ottosen et al. (2008, Eqs. 8-11) for the derivation of this equivalence. One can also show that the proposed endurance surface (12) reduces to a form similar to the Sines fatigue criterion, i.e. the equation

$$\frac{1}{2}\left[\frac{3}{2}(\boldsymbol{s}_A - \boldsymbol{s}_B) \!:\! (\boldsymbol{s}_A - \boldsymbol{s}_B)\right]^{1/2} + \\ + A_{\mathrm{L}} \bar{I}_{\mathrm{LI}} + A_{\mathrm{T}} \bar{I}_{\mathrm{TI}} - \left[(1 - \bar{\zeta}) S_{\mathrm{T}} + \bar{\zeta} S_{\mathrm{L}}\right] = 0 \tag{22}$$

corresponds to Eq. (11) in Ottosen et al. (2008), where $\bar{I}_{\mathrm{T1}} = [I_{\mathrm{T1}}(\boldsymbol{\sigma}_A) + I_{\mathrm{T1}}(\boldsymbol{\sigma}_B)]/2$, $\bar{I}_{\mathrm{L1}} = [I_{\mathrm{L1}}(\boldsymbol{\sigma}_A) + I_{\mathrm{L1}}(\boldsymbol{\sigma}_B)]/2$, and $\bar{\zeta} = [\zeta(\boldsymbol{\sigma}_A) + \zeta(\boldsymbol{\sigma}_B)]/2$. Furthermore, in uniaxial cyclic loadings, (19) takes the following form

$$\sigma_{\mathrm{a}} + \tilde{A} \tilde{I}_1 - \tilde{S}_0 = 0 \tag{23}$$

where σ_{a} is the stress amplitude and $\tilde{I}_1 := \frac{1}{2}(I_1(\sigma_A) + I_1(\sigma_B))$ is the mean value of the traces.

Fig. 5 shows damage development and movement of the endurance surface in a uniaxial loading case as the stress ranges periodically between $\sigma(A) = \sigma_{\mathrm{m}} + \sigma_{\mathrm{a}}$ and $\sigma(B) = \sigma_{\mathrm{m}} - \sigma_{\mathrm{a}}$. In such a situation, $\tilde{I}_1 = \sigma_{\mathrm{m}}$ in (23) which result

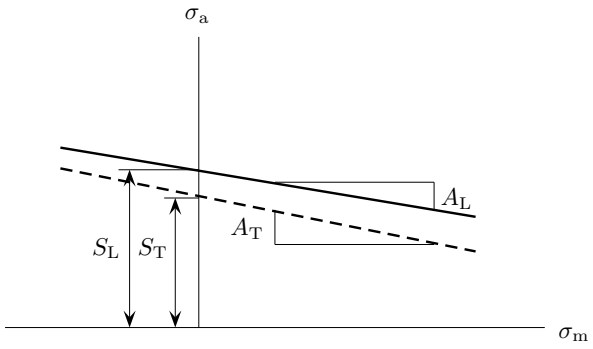

Figure 6: The endurance surface (23) in uniaxial loading is represented by the straight lines in the Haigh-diagram. Illustration of the parameters S_{L}, S_{T}, A_{L}, and A_{T} .

indicates that the variation between the fatigue stress amplitude and mean stress is linear, see Fig. 6. It is previously acknowledged that the relation (23) is in good agreement with experimental observations for many metals, cf. Forrest (1962) and Ottosen et al. (2008). However, some metals show a non-linear mean stress-amplitude relation. The difference between a linear and nonlinear relation becomes typically evident as the mean stress is greater than the stress amplitude, and the fatigue life is relatively short ($< 10^5$cycles, cf. Ottosen et al. (2008), Fig. 11). An extension of the present linear model (23) for such metals is rather straightforward, only a non-linear relation between the effective stress and the linear invariants I_{L1} and I_{T1} should be developed. Naturally, such a model requires some more material parameters to be defined.

The material parameters S_{L}, S_{T}, A_{L}, A_{T}, C, K, and L are determined using the concept analogous to that given in Ottosen et al. (2008). According to this concept, the evolution equations for the backstress and damage are integrated, and the resulting expressions are used in the calibration. The integration is split into the two parts consisting of loadings from state 1 to 2 and from state 3 to 4. During loading from state 1 to 2, damage evolves, i.e. $\beta > 0$ and $\dot{\beta} > 0$. Figure 5 then gives that $\kappa = 1$ in (18) and (19). The region between the states 2 and 3 is defined in such a manner that the stress decreases while damage and the backstress do not evolve, i.e. $\beta > 0$, $\dot{\beta} < 0$, $\dot{D} = 0$, and $\dot{\alpha} = 0$ until the stress path crosses the current endurance surface at state 3. It then follows that $\alpha_3 = \alpha_2$. From state 3 to 4, damage again evolves. In accordance with the stress path between the states 2 and 3, the damage development is inhibited until state 5 is reached, i.e. $\alpha_5 = \alpha_4$.

Based on the assumption of well defined and equal loading cycles, the endurance surface attains its periodic movement rapidly after few cycles. Due to this characteristic, $\alpha_1 = \alpha_4$. Taking advantage of (19), integration of the

equation (3) for the backstress from the state 1 to 2 yields

$$\frac{3}{2}\alpha_2 - (\tilde{A}+1)\sigma_2 + \tilde{S}_0 - \frac{S_{\mathrm{T}}}{C\tilde{A}}(\tilde{A}+1)\ln\left(\frac{1-\frac{C\tilde{A}}{S_{\mathrm{T}}}(\sigma_2-\frac{3}{2}\alpha_2)}{1-\frac{C\tilde{A}}{S_{\mathrm{T}}(\tilde{A}+1)}(\tilde{S}_0-\frac{3}{2}\tilde{A}\alpha_4)}\right)=0, \quad (24)$$

see Ottosen et al. (2008) for more detailed account. Similarly, the loading from the state 3 to 4 results in

$$-\frac{3}{2}\alpha_4 - (\tilde{A}-1)\sigma_4 + \tilde{S}_0 - \frac{S_{\mathrm{T}}}{C\tilde{A}}(\tilde{A}-1)\ln\left(\frac{1-\frac{C\tilde{A}}{S_{\mathrm{T}}}(\sigma_4-\frac{3}{2}\alpha_4)}{1-\frac{C\tilde{A}}{S_{\mathrm{T}}(\tilde{A}-1)}(\tilde{S}_0-\frac{3}{2}\tilde{A}\alpha_2)}\right)=0. \quad (25)$$

When a periodic stress state is processed, σ_2 and σ_4 are predetermined, and (24) and (25) then provide the equations for the positions α_2 and α_4 of the endurance surface.

To include the damage evolution to the model, the evolution equation (17) is integrated in similar manner as above, i.e. the integration from the state 1 to 2 yields

$$(D_2 - D_1)(1 - \frac{1}{2}(D_2 + D_1)) = \frac{K}{L}(\exp(L\beta_2) - \exp(L\beta_1)), \quad (26)$$

and from the state 3 to 4 the integration gives

$$(D_4 - D_3)(1 - \frac{1}{2}(D_4 + D_3)) = \frac{K}{L}(\exp(L\beta_4) - \exp(L\beta_3)). \quad (27)$$

Since both the state 1 and 3 are located on the endurance surface, $\beta_1 = \beta_3 = 0$, and the damage development during the entire cycle becomes

$$\Delta D := (D_2 - D_1) + (D_4 - D_3) = \frac{K}{L}\left[\frac{(\exp(L\beta_2)-1)}{(1-\frac{1}{2}(D_2+D_1))} + \frac{(\exp(L\beta_4)-1)}{(1-\frac{1}{2}(D_4+D_3))}\right]. \quad (28)$$

The damage values $D_1, ..., D_4$ are obtained comparing the left and right hand sides in (26) and (27), i.e. their expressions become

$$D_1 = D_3 = 1 - \sqrt{1 - 2\frac{K}{L}}, \quad (29)$$

$$D_2 = 1 - \sqrt{1 - 2\frac{K}{L}\exp(L\beta_2)}, \quad (30)$$

and

$$D_4 = 1 - \sqrt{1 - 2\frac{K}{L}\exp(L\beta_4)}. \quad (31)$$

Based on the assumption of complete failure, i.e. $D = 1$ after N cycles, it then follows from (28) that

$$N = \frac{L}{K}\left(\frac{\exp(L\beta_2)-1}{1-\frac{1}{2}(D_2+D_1)} + \frac{\exp(L\beta_4)-1}{1-\frac{1}{2}(D_4+D_1)}\right)^{-1}. \quad (32)$$

Substituting (19), (29), (30), and (31) into (32), taking the pairs ($\kappa = 1$, β_2) and ($\kappa = -1$, β_4) into consideration, and solving the backstresses α_2 and α_4 from (24) and (25), respectively, the number of cycles which leads to fatigue failure is obtained from (32). To calibrate the material parameters, the least squares error of number of cycles N which leads to fatigue failure is chosen as the object function. i.e.

$$f := \sum_{i=1}^{n} (w^{(i)})^2 \left(1 - \frac{\ln(N^{(i)})}{\ln(N_{\mathrm{em}}^{(i)})} \right)^2 \tag{33}$$

where n is the number of experimental points, $w^{(i)}$ are the weights, and $N^{(i)}$ and $N_{\mathrm{em}}^{(i)}$ denote the number of cycles predicted by the model and recorded in the experiments, respectively.

Based on the object function (33) and the positive parameters the minimization problem is solved by using the least squares fitting. Since under uniaxial loading with zero mean stress, the parameters S_{L} and S_{T} are nothing but the fatigue strengths in longitudinal and transverse loading direction, respectively, their values can be extracted from test data without optimization. A glance at (23) also reveals that the parameters A_{L} and A_{T} represent the slope in the Haigh-diagram as sketched in Fig. 6.

4. Experiments

Uniaxial and constant amplitude fatigue experiments for forged 34CrMo6 steel have been carried out in the directions of $\psi = 0°$, $45°$, and $90°$ in relationship to the preferred longitudinal direction. The closest equivalent AISI standard for that steel is AISI-SAE 4140, cf. Oberg et al. (1996, pp. 406-412). A standard servo-hydraulic testing machine has been used operating at 10 Hz frequency. The standard deviations of the fatigue strength data for the alignments $0°$, $90°$, and $45°$ are 3 %, 10 %, and 8 %, respectively, which values are taken into account when estimating the material parameters within such an accuracy.

The test results are shown in Fig. 8a. The material is seen to have strong directional fatigue properties: the longitudinal fatigue strength is almost 30% greater than the transverse fatigue strength. The test data is in line with preceding investigations conducted e.g. by McDiarmid (1985) and Roiko et al. (2012).

Based on data for the forged steel employed, the parameter $S_{\mathrm{T}} = 360$ MPa is first determined. The value $A_{\mathrm{L}} = 0.225$ is extracted from previously conducted experiments for varying mean stress, cf. McDiarmid (1989) and Liu and Zenner (2003). The influence of remaining parameters and weights on the objective function is shown in Fig. 7. All data points shown in Fig. 8 are used in the calibration, i.e. $n = 8$ in (33). The weights are arranged in the accordance with the loading direction and the decreasing order of the fatigue strength, i.e. the weights $w^1 - w^3$, $w^4 - w^7$, and w^8 correspond to the data points in the loading direction of $0°$, $90°$, and $45°$, respectively.

Table 1: Estimated material parameters for forged 34CrMo6 and isotropic AISI-SAE 4340 steels.

material	S_{L} [MPa]	S_{T} [MPa]	A_{L}	A_{T}	C	K	L
34CrMo6	447	360	0.225	0.300	33.6	$12.8{\cdot}10^{-5}$	4.0
AISI-SAE 4340	490	490	0.225	0.225	0.11	$1.46{\cdot}10^{-5}$	8.7

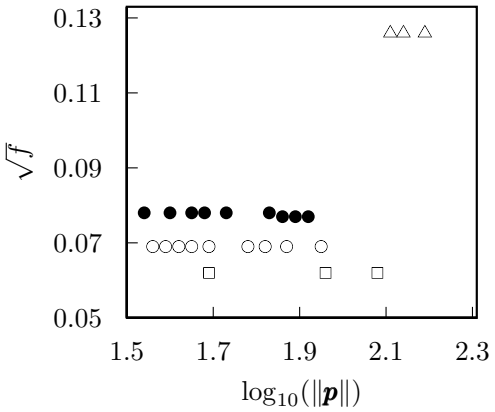

Figure 7: The influence of the weights and the parameters S_{L}, A_{T}, and $\boldsymbol{p} := \{C, \hat{K}, L\}$ on the objective within the limits of numerical tolerances employed in the optimization ($\hat{K} = 10^5 K$). Four presentative sets consisting of the fixed values $\{S_{\mathrm{L}} = 447$ MPa, $A_{\mathrm{T}} = 0.300$, $w^1 = 2.0$, $w^2 = 1.5$, $w^4 = 2.0$, $w^5 = 1.5$, $w^6 = 1.2\}$, $\{S_{\mathrm{L}} = 447$ MPa, $A_{\mathrm{T}} = 0.300$, $w^1 = 3.0$, $w^2 = 2.5$, $w^4 = 3.0$, $w^5 = 2.5$, $w^6 = 1.4\}$, $\{S_{\mathrm{L}} = 447$ MPa, $A_{\mathrm{T}} = 0.320$, $w^1 = 3.0$, $w^2 = 2.5$, $w^4 = 3.0$, $w^5 = 2.5$, $w^6 = 1.4\}$, and $\{S_{\mathrm{L}} = 440$ MPa, $A_{\mathrm{T}} = 0.285$, $w^1 = 2.0$, $w^2 = 1.5$, $w^4 = 2.0$, $w^5 = 1.5$, $w^6 = 1.2\}$, respectively, are chosen for the illustration. The results are highlighted by the markers $\square$, $\circ$, $\bullet$, and $\triangle$, respectively. The rest of the weights are equal with unity.

A small deviation in the objective function can be reached using a relative-large parameter set ranging from 1.55 to 2.10 of its logarithmic norm. Despite that the greater weights are employed, the objective function shows considerably lower values when both S_{L} and A_{T} are increased from their initial values $S_{\mathrm{L}} = 440$ MPa and $A_{\mathrm{T}} = 0.285$, respectively. The numerical investigations also indicated that low values of the remaining parameters result in more stable solution and allow longer time steps to be used in the calculations. Motivated by these observations, the values shown in Table 1 represent the best optimum solution. Table 1 shows also the optimized parameter values for an isotropic AISI-SAE 4340 steel, which material is used in Ottosen et al. (2008). However, notice that the parameters C, K and L differ from the values used in Ottosen et al. (2008) due to the difference in the adopted damage evolution equation (17). These two sets of parameters have been used in the subsequent test cases.

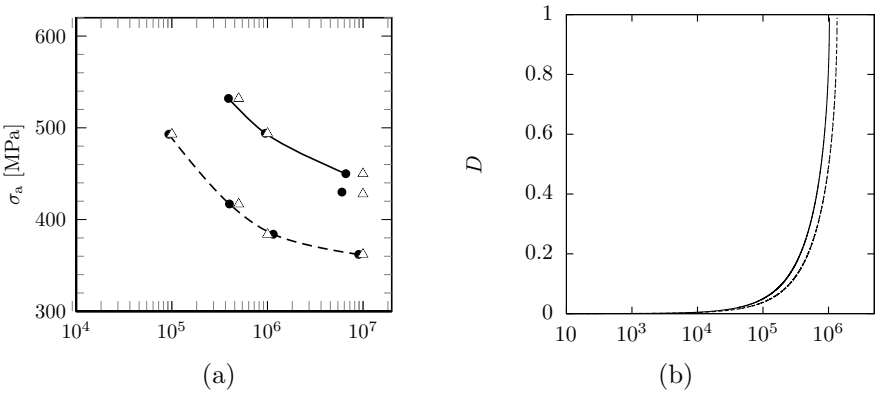

Figure 8: (a) Fatigue strengths ($\sigma_m = 0$) for the forged 34CrMo6 steel employed. The markers $\triangle$ denote the data points. The solid and dashed lines implicate the model results as the loading directions in relationship to preferred longitudinal direction are 0° and 90°, respectively. The data point (10^7,428 MPa) for the loading direction of 45° is also presented. (b) Examples of damage evolution as the loading directions are 0° (solid) and 90° (dashed).

5. Evaluation of the model

5.1. Uniaxial test cases

With the calibrated parameters given in Table 1, the predicted $S-N$ curves are shown in Fig. 8a. The load history results in the damage development represented in Fig. 8b, as the stress amplitudes σ_a are 494 MPa and 384 MPa in the preferred direction (0°) and in the transverse plane (90°), respectively. Due to the divisor employed in the evolution equation (17), the damage growth increases rapidly prior to failure, which behaviour is in line with experimental observations, cf. Lemaitre and Chaboche (1990) and Lemaitre and Desmorat (2005).

The development of the movement of the endurance surface under identical stress cycles is shown in Fig. 9. The damage evolution initiates right once as the loading is applied and the endurance surface reaches a periodic state almost immediately. This periodic state corresponds to the movement of endurance surface highlighted by the solid circles in Fig. 2. During cycling, damage always develops as the stress state is outside the endurance domain and moves away from it. This situation was already demonstrated in Fig. 5. Since the model has been calibrated to data for this alternating stress, the endurance limit strictly follows the maximal and minimal cyclic stress.

5.1.1. Effect of mean stress

In addition to stress amplitude, fatigue failure also depends on mean stress. McDiarmid (1989) investigated the influence of mean stress on fatigue life and presented test data for 34CrNiMo6 steel (British Standard EN24T). According to this test, the transverse fatigue strength in relationship to longitudinal fatigue

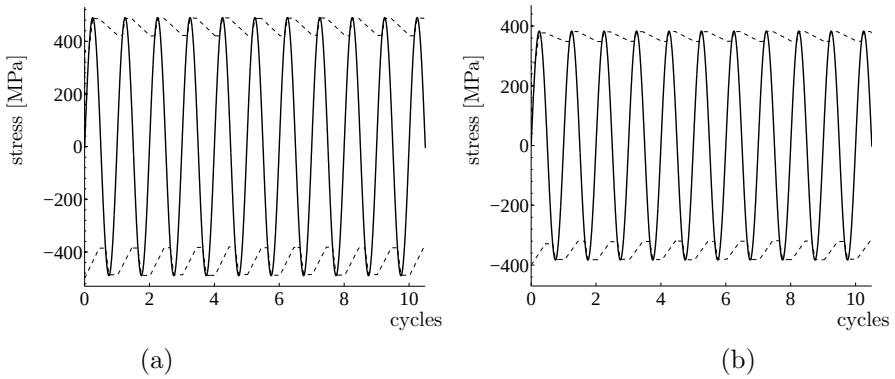

Figure 9: Development of periodic movement of the endurance surface during identically varying first few stress cycles (solid line). The endurance limit is indicated by dashed line. The loading direction is (a) parallel with and (b) perpendicular to the preferred longitudinal direction.

strength was about 80 % which result is parallel with the present experimental observations for the 34CrMo6 steel. To further evaluate the model, some Haigh-diagrams for varying mean stresses are depicted in Fig. 10. Despite the model calibration for zero mean stress, the model is able to predict the observed characteristics of fatigue strength well.

An experimentally established fact is that the fatigue limit in cyclic torsion is independent on superimposed mean torsion as the number of cycles is high (10^6 or more), and the maximum shear stress does not exceed the static yield stress, cf. e.g. Sines (1959) and Papadopoulos et al. (1997). Fig. 11a shows the predicted curves for the shear stress amplitude $\tau_{xy\mathrm{a}}$ as the mean shear stress $\tau_{xy\mathrm{m}}$ ranges from zero to $2\tau_{xy\mathrm{a}}$. All other stress components are zero. As the number of cycles is 10^6, no effect due to the mean shear stress can be observed on the fatigue life, i.e the curve tends to become horizontal. Capability of the model to predict this independence under the traceless stress state follows from the relation (23) between the fatigue stress amplitude and mean stress. However, the lower fatigue life indicates a negative slope in the $\tau_{xy\mathrm{m}} - \tau_{xy\mathrm{a}}$ interaction. Even if the interaction is weak, this characteristic corresponds to experimental observations, cf. Papadopoulos et al. (1997), Fig. 8. The model is able to predict that characteristic since the importance of mean shear stress in relationship to fatigue stress amplitude significantly increases at low fatigue lives. This effect clearly appears in the damage development shown in Fig. 11b. Compared to the damage curves of low mean shear stresses which virtually are indistinguishable, damage evolves rapidly under the shear mean stress $\tau_{xy\mathrm{m}} = 2\tau_{xy\mathrm{a}}$ and reaches about 40 % of its limit before the periodic stress state is achieved.

5.2. Multiaxial stress state

Multiaxial stress states typically occur at the most stressed locations prior to failure. The stress components may mutually vary at different frequencies and

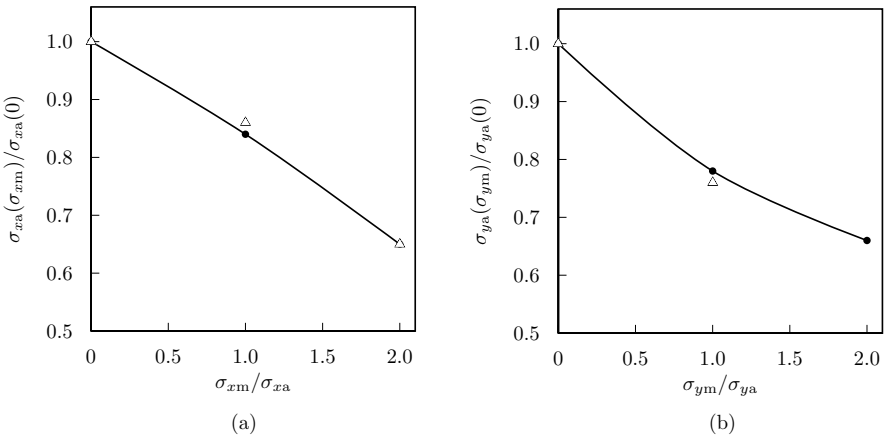

Figure 10: Effect of mean stress on fatigue life of 10^6 cycles under (a) longitudinal and (b) transverse uniaxial cyclic tension. The x-coordinate direction is parallel with the preferred longitudinal direction. Available experimental data for 34CrNiMo6 (BS EN24T) steel depicted by the markers $\triangle$ is taken from McDiarmid (1989).

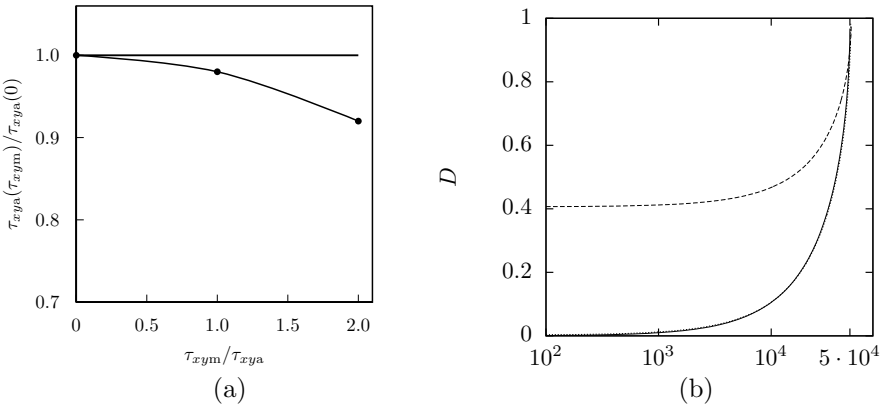

Figure 11: (a): Effect of mean shear stress on the fatigue strength as the number of cycles is $N = 10^6$ (solid line) and $N = 5 \cdot 10^4$ (solid line with dots). (b): Damage evolution during $5 \cdot 10^4$ cycles as $\tau_{xym} = 0$ (solid line), $\tau_{xym} = \tau_{xya}$ (dotted line), and $\tau_{xym} = 2\tau_{xya}$ (dashed line).

magnitudes. In order to use the model in multiaxial loadings, the analytical formulas (24), (25), and (32) cannot be applied, and therefore a numerical approach has to be developed so as to integrate the evolution equations (3) and (17) for the backstress and damage, respectively. Taking advantage of (3),

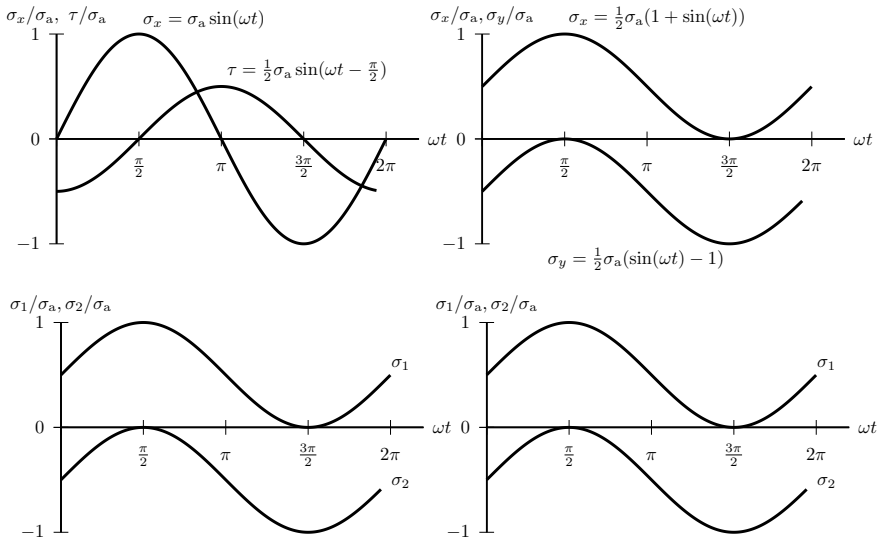

Figure 12: (Upper) Alternating normal stress combinations for one cycle. The phase differences are $\phi_{xy} = \pi/2$ and $\phi_x = \phi_y = 0$. (Below) Corresponding principal stresses.

(8), and (9), the time rate of the endurance surface (12) can be expressed as a function of the stress rate as

$$\dot{\beta} = \frac{1}{S_{\mathrm{T}} + C\bar{\sigma}} \left[\frac{\frac{3}{2}(\boldsymbol{s} - \boldsymbol{\alpha})}{\bar{\sigma}} + (A_{\mathrm{L}} - A_{\mathrm{T}})\boldsymbol{B} + A_{\mathrm{T}}\boldsymbol{I} \right. \\ \left. - \frac{(S_{\mathrm{L}} - S_{\mathrm{T}})}{2I_2^2} \left(I_2(4\boldsymbol{\sigma} - 2I_4\boldsymbol{I})\boldsymbol{B} - (2I_5 - I_4^2)\boldsymbol{\sigma} \right) \right] \!:\! \dot{\boldsymbol{\sigma}} \quad (34)$$

When the conditions (5) are fulfilled, numerical time integration is used to solve the backstress (3), damage (17), and the endurance surface (34), which equations govern the high-cycle fatigue process.

5.2.1. Stress states of identically alternating principal stresses

It is well known that classical failure criteria which rely on purely stress invariants cannot differentiate multiaxial stress histories having equivalent principal stresses. Fig. 12 illustrates two such loadings. While classical multiaxial approaches result in the same equivalent stress for both cases, experiments show considerably different endurance limits. Due to the backstress involved in the equivalent stress (12), the fatigue strength ratios $\sigma_{xa}(\phi_y = 0°)/\sigma_{xa}(\phi_{xy} = 90°)$ for the two steels presented in Table 1 become 1.9 and 1.7, respectively, i.e. the fatigue limits differ significantly between the loading situations. Similar effect is also observed in smooth specimens made of a steel considered as isotropic, cf. e.g. Liu and Zenner (2003).

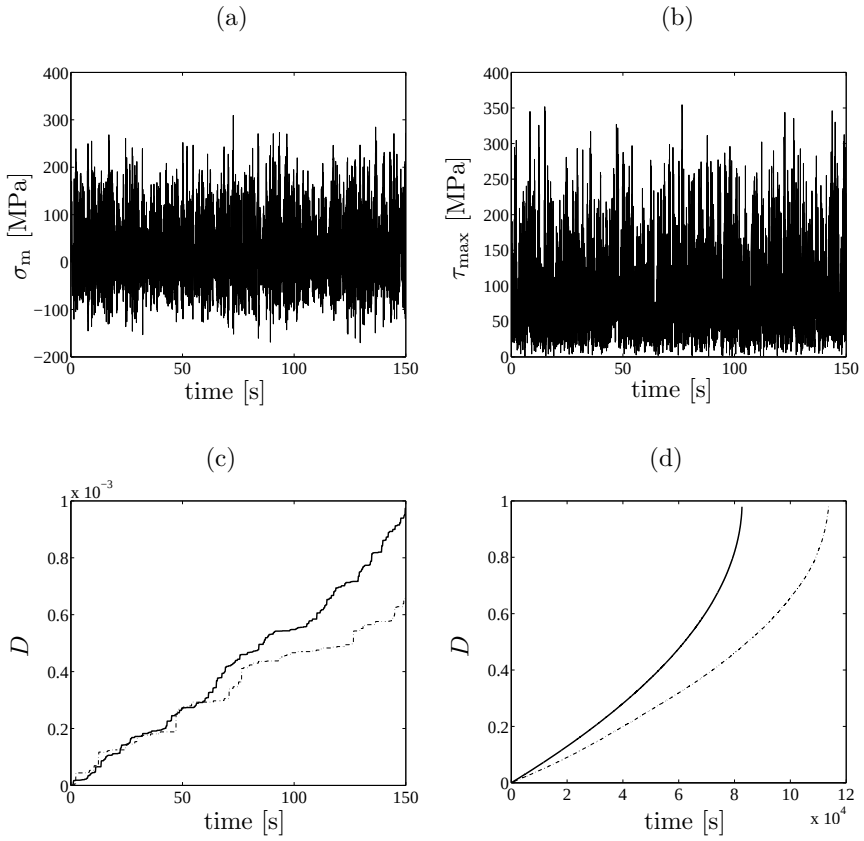

Figure 13: (a) The mean stress and (b) maximun shear stress history of a 3D-random loading. (c) The initial and (d) total fatigue damage development of the forged 34CrMo6 steel and AISI-SAE 4340 steel are highlighted by the solid and dash-and-dot line, respectively.

5.2.2. Complex loading

It also is interesting to investigate three dimensional complex cyclic loads in order to take advantage of the incremental formulation of the proposed model. The time history for all six stress components is randomly generated assuming the stresses vary between the limits −340 MPa and 580 MPa. During the whole stress history, the von Mises stress is well below the yield stress (over 700 MPa) for both steels applied, which can also be concluded from the clip of the maximum shear stress history shown in Fig. 13b. From a mesoscopic point of view, the final fatigue damage at the supposed, emerging crack tips is acknowledged to be a consequence of plastic deformation zones, see Lemaitre (1984), Suresh (1998), and Morel et al. (2001). At this phase, however, majority of the material remains elastic as it is assumed in the HCF-analysis.

The model was implemented in a Fortran program by using the backward Euler integration scheme. Computations were conducted by a Intel Haswell processor running at 2.6 GHz. To capture accurately the damage evolution

under the given complex load spectrum, small time steps of 0.03 second were used. Due to this small time step employed, the Newton's iteration needed in average only one corrector iteration per a time step to converge within the absolute tolerance of 10^{-8} for the Euclidean norm of the residual vector. The computation up to the final failure ($D = 1$) took 40-50 seconds of CPU time.

The damage development for both the calibrated steels, 34CrMo6 and AISI-SAE 4340, see Table 1, is shown in Fig. 13c-d. A significant interest is that the proposed evolution equations based fatigue model readily predicts the damage development under the multiaxial complex loading without the need of cycle counting techniques frequently applied in fatigue analyses. Rate of the damage evolution accelerates towards the end of the lifetime which is the case for most of the metallic materials, see Lemaitre and Chaboche (1990) and Lemaitre and Desmorat (2005).

The model was also implemented in a finite element program for the investigations of the fatigue damage behavior under two and three dimensional load histories, see Holopainen et al. (2015). Computations under those conditions well confirm the expected fatigue damage development and verify the model's capability under multiaxial loading conditions.

5.2.3. Effect of phase difference

For further assessing the performance of the model under multiaxial stress states, the effect of a phase shift between an alternating shear and normal stresses is investigated. In all cases, the stress waveform is sinusoidal. Considering first biaxial alternating normal stresses given by

$$\begin{aligned} \sigma_x &= \sigma_{x\mathrm{m}} + \sigma_{x\mathrm{a}} \sin(\omega t), \\ \sigma_y &= \sigma_{x\mathrm{m}} + \sigma_{x\mathrm{a}} \sin(\omega t - \phi_y). \end{aligned} \tag{35}$$

The mean stress $\sigma_{x\mathrm{m}} = 1.105\sigma_{x\mathrm{a}}$ is defined by the ratio $R = 0.05$ between the smallest and largest normal stresses. Considering first the isotropic model predictions for AISI-SAE 4340 steel, cf. Table 1. Once the phase difference $\phi_y = 30°$ is passed, the model predicts an increase of the fatigue strength followed by a strong decrease of about 30 %, which corresponds well with the experimental data of Liu and Zenner (2003), cf. Fig. 14a.

McDiarmid (1989) conducted tests on thin wall tubular specimens made of 34CrNiMo6 (BS EN24T) steel which shows strong directional fatigue properties. Compared to the zero shift, the fatigue strength under the phase difference of 180° was shown to be about 25 % lower, which result is virtually equal with the model result using the estimated 34CrMo6 steel properties. The test results in McDiarmid (1989) also indicated that the influence of the fatigue strength on this reduction is low.

Fig. 14b shows also the effect of a phase difference between a fully reversed shear stress and normal stress which pulsates in the preferred longitudinal direction as already depicted in Fig. 12 (left), i.e.

$$\begin{aligned} \sigma_x &= \sigma_{x\mathrm{a}} \sin(\omega t) \\ \tau_{xy} &= \tfrac{1}{2}\sigma_{x\mathrm{a}} \sin(\omega t - \phi_{xy}). \end{aligned} \tag{36}$$

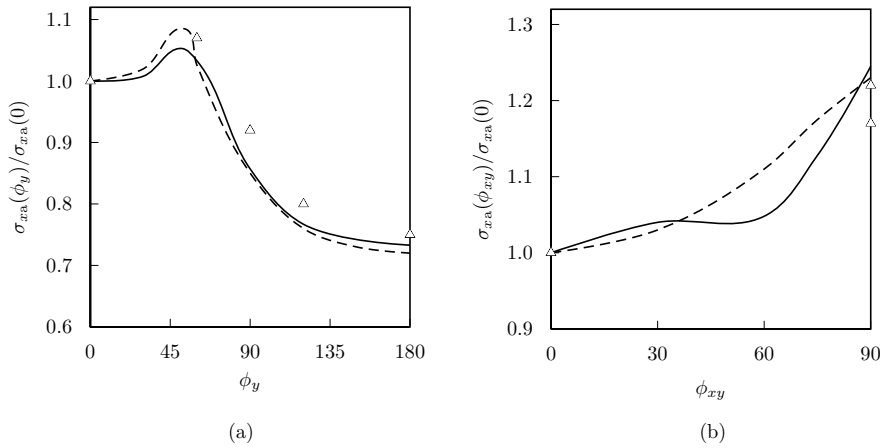

Figure 14: (a) Influence of phase shift on the fatigue strength under two cyclic normal stresses. (b) Influence of phase shift between a cyclic normal and a shear stress. The solid and dashed line denote the transversely isotropic and isotropic model predictions, respectively. The preferred longitudinal direction coincides with the x-axis. Data points △ for 42CrMo4 steel are taken from Liu and Zenner (2003).

Due to the symmetry, only the phase shifts up to $\phi_{xy} = 90°$ are presented. The phase difference results in a relative-strong increase in the fatigue strength within the range from 60° to 90°. Comparison to data for isotropic metallic solids reveals that similar albeit lower effect can also be observed from the phase shift $\phi_{xy} = 30°$, cf. Liu and Zenner (2003). Since the x-coordinate direction is now parallel with the preferred longitudinal direction, the parameter ζ in (12) is unity and the invariant I_{T1} vanishes, thus the transverse isotropic endurance surface reduces to the isotropic one, cf. equation (1). Due to this reason, the model prediction is also in good agreement with preceding data for isotropic steels, cf. Liu and Zenner (2003). According to their experiments, however, this effect is not uniform, i.e. different fatigue strength values are observed in the phase shifts from 60°.

5.2.4. Effect of frequency difference

Due to uniaxial loadings employed in the experiments, the influence of stress frequency on the fatigue strength is considered small and is typically neglected. In multiaxial loading situations, however, the effect of frequency difference between the stress components can be significant and needs an attention.

A stress state consisting of the following two alternating nonzero stress components is considered first:

$$\begin{aligned} \sigma_x &= \sigma_{xa} \sin(\omega_x t) \\ \tau_{xy} &= \tfrac{1}{2}\sigma_{xa} \sin(\omega_{xy} t). \end{aligned} \tag{37}$$

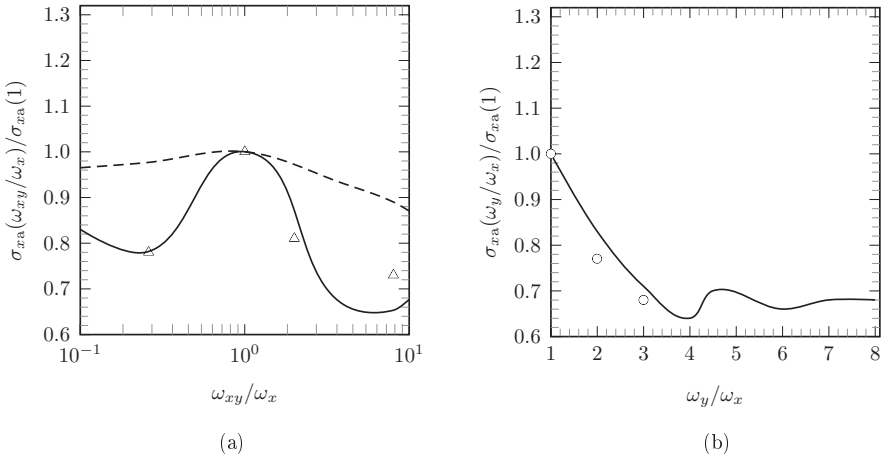

Figure 15: (a) Influence of frequency difference on the fatigue strength as the stress state consists of cyclic normal and shear stresses. The dashed line refers to the isotropic model results for the AISI-SAE 4340 steel. (b) Influence of frequency difference between two cyclic normal stresses. The markers △ and ∘ denote the data points for 25CrMo4 and 34CrNiMo6 steel taken from Mielke (1980) and McDiarmid (1989), respectively. The x-coordinate direction is parallel with the preferred longitudinal direction. The solid line indicates the transversely isotropic model response.

Fig. 15a illustrates the fatigue strength diagrams for both materials given in Table 1. For a comparison, the experimental results for 25CrMo4 steel taken from Mielke (1980) are also presented (also given in Liu and Zenner (2003)). Meanwhile the response of the transversely isotropic fatigue model fits well to data, the isotropic model response shows much higher values for the fatigue strength. This could suggest that the steel used in those tests have had anisotropic fatigue properties.

Finally, the model response for the two alternating normal stresses given by

$$\begin{aligned} \sigma_x &= \sigma_{xa}\sin(\omega_x t) \\ \sigma_y &= \sigma_{xa}\sin(\omega_y t) \end{aligned} \tag{38}$$

is considered. Steel material which is used for a comparison is 34CrNiMo6 (BS EN24T) steel showing also transverse isotropic fatigue properties, cf. McDiarmid (1989). The comparison between the model response and data is shown in Fig. 15b. Despite a slight difference between steels, the model predicts the effect of stress frequency relatively well.

6. Conclusions

An extension of the Ottosen et al. (2008) model which is suitable for the modelling of high-cycle fatigue of materials having transversely isotropic fatigue properties is proposed. The model is suitable for arbitrary multiaxial load

histories. Alike to the original model, the evolution equations are formulated in the rate form without the need to measure damage changes per cycle. Moreover, the model does not require any specific strategy, such as cycle-counting, when modelling fatigue under multiaxial stress states. In contrast to the original approach, the damage evolution is increasingly cumulative prior to failure, which characteristic is in line with experimental observations.

Evolution of high cycle fatigue is governed by an endurance function suitable in multiaxial stress states for transverse isotropic fatigue. The key issue in the development of the endurance function is the definition of the privileged direction and its perpendicular isotropic plane. Based on a structural tensor for transverse isotropy, the stress is split into the two components corresponding the stress in a transversal isotropy plane and the remaining part characterized by the longitudinal material direction, respectively. The two stress components allow to define relevant invariants needed to obtain the endurance function suitable for transverse isotropic fatigue. This conceptual approach, which is applied to the proposed model, is believed to be the simplest possible one for modelling transversely isotropic high-cycle fatigue.

The model has been calibrated to data for uniaxial fully reversed cyclic stresses acting at the three directions 0°, 90°, and 45° in relationship to the preferred longitudinal direction. Despite the calibration to uniaxial test data for zero mean stress, a comparison to data and preceding studies indicated that the proposed model predicts the fatigue behaviour under nonzero mean stress well. It was also shown that the model is able to cover multiaxial out-of-phase and asynchronous load conditions observed by test data of steels having both isotropic and transversely isotropic fatigue properties. In addition, the model captures also the effect from rotation of the principal stresses to the fatigue strength as well as the subtle effect of mean shear stress on the fatigue strength in cyclic torsion.

An important aspect of this work is the applicability of the proposed model for applications in practise. From this point of view, the model has been kept as simple as possible. However, since cracking inevitably leads to anisotropic elastic behaviour, an anisotropic damage model should be developed. More data which account for directional high-cycle fatigue is also needed. Temperature effects on the fatigue strength as well as a model extension to low-cycle fatigue regime are also important supplements to be involved in future research.

Acknowledgements

This work has been supported in part by Tekes - the National Technology Agency of Finland, project SCarFace, decision number 40205/12.

References

Arnold, S., Kruch, S., 1991. Differential continuum damage mechanics models for creep and fatigue of unidirectionla metal matrix composites. Technical Report 105213. NASA Technical Memorandum 105213.

Askes, H., Livieri, P., Susmel, L., Taylor, D., Tovo, R., 2012. Intrinsic material length, Theory of Critical Distances and Gradient Mechanics: analogies and differences in processing linear-elastic crack tip stress fields. Fatigue & Fracture of Engineering Materials & Structures 36, 39–55. doi:10.1111/j.1460-2695.2012.01687.x.

Boehler, J., 1987. Yielding and failure of transversely isotropic solids. Springer-Verlag. chapter 5. Number 292 in International Centre for Mechanical Sciences, Courses and Lectures, Applications of Tensor Functions in Solid Mechanics, pp. 67–97.

Bolotin, V., 1999. Mechanics of Fatigue. CRC Mechanical Engineering Series, CRC Press, Boca Raton.

Brighenti, R., Carpinteri, A., Corbari, N., 2013. Damage mechanics and paris regime in fatigue life assessment of metals. International Journal of Pressure Vessels and Piping 104, 57 – 68. doi:http://dx.doi.org/10.1016/j.ijpvp.2013.01.005.

Carpinteri, A., Spagnoli, A., 2001. Multiaxial high-cycle fatigue criterion for hard metals. International Journal of Fatigue 23, 135 – 145. doi:10.1016/S0142-1123(00)00075-X.

Dang Van, K., 1993. Macro-micro approach in high-cycle multiaxial fatigue, in: McDowell, D. (Ed.), Advances in Multiaxial Fatigue, Americal Society for Testing and Materials, Philadelphia. pp. 120–130.

Dang Van, K., Gailletaud, G., Flavenot, G., Le Douaron, A., Lieurade, H., 1989. Criterion for high cycle fatigue failure under multiaxial loading, in: Brown, M., Miller, K. (Eds.), Biaxial and Multiaxial Fatigue, Mechanical Engineering Publications, London. pp. 459–478.

Desmorat, R., Kane, A., Seyedi, M., Sermage, J., 2007. Two scale damage model and related numerical issues for thermo-mechanical high cycle fatigue. European Journal of Mechanics - A/Solids 26, 909 – 935. doi:http://dx.doi.org/10.1016/j.euromechsol.2007.01.002.

Ding, X., He, G., Chen, C., Zhu, Z., Liu, X., Crepeau, P., 2007. A brief review of multiaxial high-cycle fatigue. Metallurgical and Materials Transactions B 38B, 591–599. doi:10.1007/s11663-007-9021-x.

Findley, W., 1959. A theory for the effect of mean stress on fatigue of metals under combined torsion and axial load or bending. Journal of Engineering for Industry , 301–306.

Forrest, P., 1962. Fatigue of metals. Pergamon Press.

Holopainen, S., Kouhia, R., Könnö, J., Saksala, T., 2015. Computational modelling of high-cycle cycle fatigue using a continuum based model., in: Berezovski, A., Tamm, K., Peets, T. (Eds.), Proc. Of the 28th Nordic Seminar on

Computational Mechanics, 22-23 October, 2015, Tallinn, Estonia, Institute of Cybernetics at Tallinn University of Technology. pp. 71–74.

Kenmeugne, B., Soh Fotsing, B., Anago, G., Fogue, M., Roberts, J.L., Kenne, J.P., 2012. On the evolution and comparison of multiaxial fatigue criteria. International Journal of Engineering and Technology 4, 37–46. URL: http://www.enggjournals.com/ijet/docs/IJET12-04-01-015.pdf.

Kruch, S., Arnold, S., 1997. Creep damage and creep-fatigue damage interaction model for unidirectional metal-matrix composites, in: McDowell, D. (Ed.), Applications of Continuum Damage Mechanics to Fatigue and Fracture, ASTM. pp. 7–28.

Lemaitre, J., 1984. How to use damage mechanics. Nuclear Engineering and Design 80, 233–245.

Lemaitre, J., Chaboche, J.L., 1990. Mechanics of Solid Materials. Cambridge University Press.

Lemaitre, J., Desmorat, R., 2005. Engineering Damage Mechanics, Ductile, Creep, Fatigue and Brittle Failures. Springer-Verlag, Berlin, Heidelberg.

Liu, J., Zenner, H., 2003. Fatigue limut of ductile metals under multiadial loading, in: Carpinteri, A., de Freitas, M., Spagnoli, A. (Eds.), Biaxial/multiaxial fatigue and fracture, Elsevier Science Ltd. and ESIS. pp. 147–163.

Liu, Y., Mahadevan, S., 2007. A unified multiaxial fatigue damage model for isotropic and unisotropic materials. International Journal of Fatigue 29, 347–359.

Lorand, K., 2012. Review of high-cycle fatigue lodels applied for multiaxial tension-torsion loading based on a new accuracy assesment parameter. Journal of Engineering Studies and Research 18, 75–86.

Luu, D., Maitournam, M., Nguyen, Q., 2014. Formulation of gradient multiaxial fatigue criteria. International Journal of Fatigue 61, 170–183. doi:10.1016/j.ijfatigue.2013.11.014.

Makkonen, L., Rabb, R., Tikanmäki, M., 2014. Size effect in fatigue based on the extreme value distributions of defects. Materials Science & Engineering A 594, 68–71. doi:10.1016/j.msea.2013.11.045.

Matake, T., 1977. An explanation on fatigue limit under combined stress. Bulletin of the Japan Society of Mechanical Engineers 20, 257–263.

McDiarmid, D., 1985. Fatigue under out of phase biaxial stresses of different frequences, in: Miller, K., Brown, M. (Eds.), Multiaxial Fatigue, ASTM STP 853, ASTM, Philadelphia, PA. pp. 606–621.

McDiarmid, D., 1989. Effect of mean stress on biaxial fatigue where stresses are out-of-phase and at different frequences, in: Brown, M., Miller, K. (Eds.), Biaxial and Multiaxial Fatigue, EGF3, London. pp. 605–619.

McDowell, D., 1996. Basic issues in the mechanics of high cycle metal fatigue. International Journal of Fracture 80, 103–145. doi:10.1007/BF00012666.

Mielke, S., 1980. Festigkeitsvarhalten metallischer Werkstoffe unter zweiachsig schwingender Beanspruchung mit verchiedenen Spannungszeitverläufen. Ph.D. thesis. RWTH Aachen.

Morel, F., 2001. A critical plane fatigue model applied to out-of-phase bending and torsion load conditions. Fatigue & Fracture of Engineering Materials & Structures 24, 153–164. doi:10.1046/j.1460-2695.2001.00390.x.

Morel, F., Palin-Luc, T., Froustey, C., 2001. Comparative study and link between mesoscopic and energetic approaches in high cycle multiaxial fatigue. International Journal of Fatigue 23, 317–327. doi:10.1016/S0142-1123(00)00100-6.

Murakami, S., 2012. Continuum Damage Mechanics. volume 185 of *Solid Mechanics and Its Applications*. Springer Netherlands.

Murakami, Y., 2002. Metal Fatigue, Effects of Small defects and Nonmetallic Inclusions. Elsevier Science.

Oberg, E., Jones, F., Horton, H., Ryffel, H. (Eds.), 1996. Machinery's Handbook. 25 ed., Industrial Press Inc.

Ottosen, N., Stenström, R., Ristinmaa, M., 2008. Continuum approach to high-cycle fatigue modeling. International Journal of Fatigue 30, 996–1006. doi:10.1016/j.ijfatigue.2007.08.009.

Paas, M., Schreurs, P., Brekelmans, W., 1993. A continuum approach to brittle and fatigue damage. International Journal of Solids and Structures 30, 579–599.

Palin-Luc, T., Lasserre, S., 1998. An energy based criterion for high cycle multiaxial fatigue. European Journal of Mechanics - A/Solids 17, 237 – 251. doi:http://dx.doi.org/10.1016/S0997-7538(98)80084-3.

Papadopoulos, I., Davoli, P., Gorla, C., Filippini, M., Bernasconi, A., 1997. A comparative study of multiaxial high-cycle fatigue criteria for metals. International Journal of Fatigue 19, 219–235. doi:10.1016/S0142-1123(96)00064-3.

Papadopoulos, I.V., 2001. Long life fatigue under multiaxial loading. International Journal of Fatigue 23, 839 – 849. doi:10.1016/S0142-1123(01)00059-7.

Peerlings, R., Brekelmans, W., de Borst, R., Geers, M., 2000. Gradient-enhanced damage modelling of high-cycle fatigue. International Journal for Numerical Methods in Engineering 49, 1547–1569. doi:10.1002/1097-0207(20001230)49:12<1547::AID-NME-16>3.0.CO;2-D.

Robinson, D., Binienda, W., Miti-Kavuma, M., 1990. Creep and creep rupture of strongly reinforced metallic composites. Contractor Report 185286. NASA. Lewis Research Center.

Robinson, D., Duffy, S., 1990. Continuum deformation theory for high-temperature metallic composites. Journal of the Engineering Mechanics, ASCE 116, 832–844. doi:10.1061/(ASCE)0733-9399(1990)116:4(832).

Roiko, A., Hänninen, H., Vuorikari, H., 2012. Anisotropic distribution of non-metallic inclusions in a forged steel roll and its influence on fatigue limit. International Journal of Fatigue 41, 158–167.

Sines, G., 1955. Failure of materials under combined repeated stresses with superimposed static stresses. Technical Report 3495. NACA. Washington, USA.

Sines, G., 1959. Behavior of metals under complex stresses. McGraw-Hill. pp. 145–169.

Socie, D., Marquis, G., 2000. Multiaxial Fatigue. Society of Automotive Engineers, Inc., Warrendale, Pa.

Suresh, S., 1998. Fatigue of Materials. 2nd ed., Cambridge University Press.

Wang, Y.Y., Yao, W.X., 2004. Evaluation and comparison of several multiaxial fatigue criteria. International Journal of Fatigue 26, 17 – 25. doi:10.1016/S0142-1123(03)00110-5.

Zhang, L., Liu, X., Wang, L., Wu, S., Fang, H., 2012. A model of continuum damage mechanics for high cycle fatigue of metallic materials. Transactions of Nonferrous Metals Society of China 22, 2777–82. doi:10.1016/S1003-6326(11)61532-X.

Zouain, N., Cruz, I., 2002. A high-cycle fatigue criterion with internal variables. European Journal of Mechanics - A/Solids 21, 597 – 614. doi:http://dx.doi.org/10.1016/S0997-7538(02)01227-5.

Zouain, N., Mamiya, E.N., Comes, F., 2006. Using enclosing ellipsoids in multiaxial fatigue strength criteria. European Journal of Mechanics - A/Solids 25, 51 – 71. doi:http://dx.doi.org/10.1016/j.euromechsol.2005.07.006.